Article

Structure

Parallel Evolution of Chemokine Binding by Structurally Related Herpesvirus Decoy Receptors

Graphical Abstract

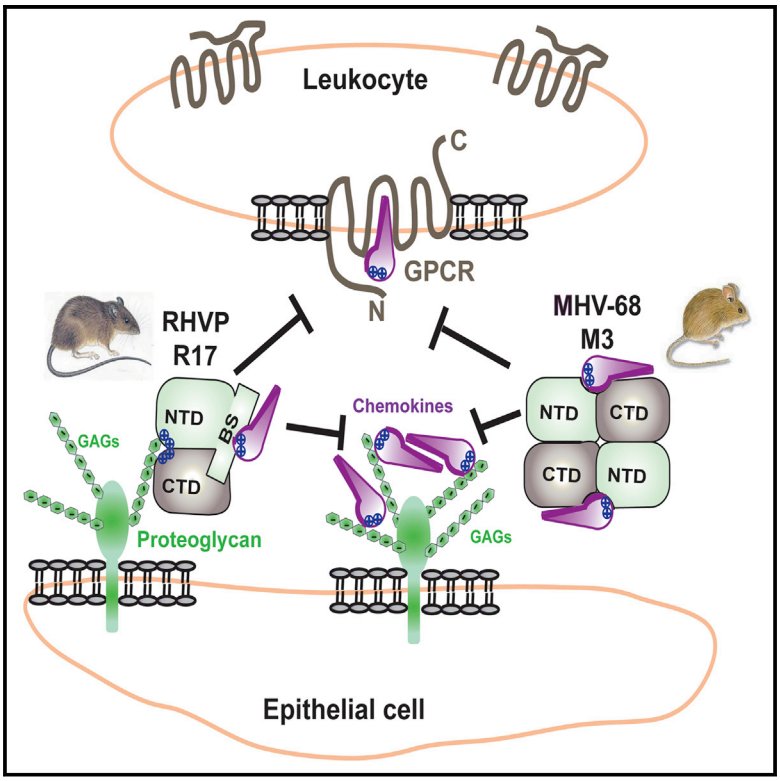

Authors

Olga Y. Lubman, Daved H. Fremont

Correspondence

fremont@wustl.edu

In Brief

Lubman and Fremont describe the atomic structure of the herpesvirus-encoded chemokine binding protein R17 alone and in complex with a high-affinity ligand, CCL3. The study offers novel insights into the conserved and unique mechanisms that different pathogens use to undermine host chemokine signaling networks.

Highlights

- Crystal structures of RHVP R17 alone and in complex with CCL3 have been determined
- R17 is similar to MHV-68 M3 although the location of chemokine binding is distinct
- Chemokine residues that stabilize R17 complexes have been mapped by mutagenesis
- Pathogen decoys mimic GPCRs in engagement of invariant chemokine determinants

Lubman & Fremont, 2016, Structure *24*, 57–69
January 5, 2016 ©2016 Elsevier Ltd All rights reserved
http://dx.doi.org/10.1016/j.str.2015.10.018

Structure
Article

Parallel Evolution of Chemokine Binding by Structurally Related Herpesvirus Decoy Receptors

Olga Y. Lubman[1] and Daved H. Fremont[1,2,3,*]
[1]Department of Pathology and Immunology, Washington University School of Medicine, St. Louis, MO 63110, USA
[2]Department of Biochemistry and Molecular Biophysics, Washington University School of Medicine, St. Louis, MO 63110, USA
[3]Department of Molecular Microbiology, Washington University School of Medicine, St. Louis, MO 63110, USA
*Correspondence: fremont@wustl.edu
http://dx.doi.org/10.1016/j.str.2015.10.018

SUMMARY

A wide variety of pathogens targets chemokine signaling networks in order to disrupt host immune surveillance and defense. Here, we report a structural and mutational analysis of rodent herpesvirus Peru encoded R17, a potent chemokine inhibitor that sequesters CC and C chemokines with high affinity. R17 consists of a pair of β-sandwich domains linked together by a bridging sheet, which form an acidic binding cleft for the chemokine CCL3 on the opposite face of a basic surface cluster that binds glycosaminoglycans. R17 promiscuously engages chemokines primarily through the same N-loop determinants used for host receptor recognition while residues located in the chemokine 40s loop drive kinetically stable complex formation. The core fold adopted by R17 is unexpectedly similar to that of the M3 chemokine decoy receptor encoded by MHV-68, although, strikingly, neither the location of ligand engagement nor the stoichiometry of binding is conserved, suggesting that their functions evolved independently.

INTRODUCTION

Chemokines are a group of small cytokines that orchestrate host defense against microorganisms in vertebrates (Esche et al., 2005; Gerard and Rollins, 2001). Pro-inflammatory chemokines play an essential role in the clearance of a broad array of pathogens through the recruitment of effector leukocytes (Luster, 1998). Chemokines establish gradients through specific interactions with glycosaminoglycans (GAGs), and direct target cell migration and activation by binding to G-protein-coupled chemokine receptors (Allen et al., 2007; Handel et al., 2005). Chemokine networks are characterized by ligand-receptor promiscuity, antagonistically acting ligands, and non-signaling decoy receptors (Allen et al., 2007; Fernandez and Lolis, 2002; Handel and Lau, 2004). All chemokines adopt a similar fold consisting of an extended N terminus followed by a long flexible loop (N loop), a three-stranded β sheet, and a C-terminal α helix (Fernandez and Lolis, 2002). The structural determinants of chemokine G-protein-coupled receptor (GPCR) recognition have recently been illuminated by studies of CXCR4 in complex with a herpesvirus-encoded chemokine and CX3CL1 in complex with a herpesvirus-encoded chemokine receptor (Burg et al., 2015; Qin et al., 2015). Receptor activation is thought to occur in several steps whereby initial binding of the chemokine N loop causes conformational changes in the receptor, allowing the N-terminal residues of the chemokine to insert between transmembrane helices of the GPCR (Kufareva et al., 2015).

Pathogens undermine host chemokine signaling networks using a number of different strategies. Large DNA viruses, such as herpes- and poxviruses, encode versions of chemokines, chemokine receptors, and unique soluble chemokine binding proteins capable of sequestering host chemokines with distinct specificity (Alcami, 2003; Alcami and Lira, 2010; Epperson et al., 2012). The first secreted chemokine decoy receptor was discovered in orthopoxviruses, and it is now established that a wide array of chemokine binding proteins are encoded by poxviruses (Patel et al., 1990; Smith et al., 1997). Unique chemokine binding proteins had been identified in all three subfamilies of herpesviruses, with perhaps the best characterized being M3 encoded by mouse gammaherpesvirus 68 (MHV-68) (Heidarieh et al., 2015). Bloodsucking ticks and the helminth parasite *Schistosoma mansoni* have also been shown to produce chemokine binding proteins (Deruaz et al., 2008; Smith et al., 2005).

We recently discovered a novel chemokine decoy receptor encoded by rodent herpesvirus Peru (RHVP) (Lubman et al., 2014). RHVP is a gammaherpesvirus (rhadinovirus)-related to MHV-68 (Stevenson and Efstathiou, 2005) and Kaposi's sarcoma-associated herpesvirus (Lee et al., 2015) that establishes acute and latent infection in laboratory mice with overt pathology evident only in immunocompromised animals (Loh et al., 2011). We demonstrated that R17 binds all human and murine CC and C chemokines tested (mCCL2 and hCCL2; mCCL3 and hCCL3; mCCL4, mCCL5, and hCCL5; mCCL8, mCCL11, mCCL20, mCCL24, mCCL19, mCCL12, and mXCL1) but not any of the CXC or CX3C chemokines (mCXCL8, mCXCL10, mCXCL9, mCXCL2, mCXCL12, mCXCL1, and CX3C). Functionally, recombinant R17 potently inhibits CCL3-driven chemotaxis of human peripheral blood mononuclear cells (PBMCs) and CCL2-driven transmigration of human THP-1 monocytes

Table 1. Crystallographic Data Collection and Refinement Statistics

	R17_native	R17_KI_derivative 1	R17_KI_derivative 2	R17 (KI_ merged)	R17-CCL3 complex
Data Collection					
Source	APS_23ID	ALS 4.2.2	ALS 4.2.2		ALS 4.2.2
Wavelength (Å)	1.0	1.77	1.77		1.0
Resolution (Å)	50–1.9 (1.93–1.90)	50–2.64 (2.69–2.64)	50–2.90 (2.94–2.90)	90–2.64	50–3.0 (3.06–3.00)
No. of observations	281,521	685,862	641,455	45,751	826,635
Unique reflections	45,516	17,071	13,291	16,547	26,825
Redundancy	3 (2.8)	13.8 (9.7)	13.8 (12.0)	2.8 (1.0)	4.7 (2.3)
$I/\sigma I$	20.8 (1.83)	39.04 (3.05)	26.9 (2.4)	17.8 (2.7)	7.4 (1.0)
R_{merge}[a]	5.2 (65.4)	6.8 (83.1)	11.7 (100)	2.1 (100)	11.2 (100)
Completeness	93.8 (61.2)	99.8 (97.6)	100 (100)	970 (56.8)	100 (64.8)
Space group	$P2_12_12_1$	$P2_12_12_1$	$P2_12_12_1$	$P2_12_12_1$	I222
Cell dimensions (Å)	69.5, 75.8, 106.9	69.5, 75.3, 106.1	69.5, 76.0, 107.6		98.4, 109.4, 210.9
Phasing Statistics					
No. of iodides (SHELXD)				14	
Figure of merit (centric)				0.22	
Figure of merit (acentric)				0.27	
Phasing resolution				46–3.10	
R_{cullis}				0.79	
Refinement Statistics					
Resolution (Å)	50–1.9				50–3.0
(outer shell) (Å)	(1.94–1.89)				(3.08–3.0)
No. of reflections/no. in R_{free}	39,897/2,024				24,120/1,817
R_{cryst} (%)	18.44 (22.3)				21.52 (32.9)
R_{free} (%)	22.08 (34.2)				27.40 (45.5)
Rmsd bond lengths	0.005				0.003
Rmsd bond angles	0.992				0.462
Ramachandran favored (%)	95.6				94.2
Ramachandran outliers (%)	0.0				0.0
Average *B* factor	21.65				66.92
PDB ID	4ZKQ				4ZLT

Numbers in parentheses refer to the highest-resolution shell.
[a]$R_{merge} = \Sigma|I - \langle I\rangle|/\Sigma\langle I\rangle$, where I is the intensity of each individual reflection.

(Lubman et al., 2014). Our initial studies also revealed that in addition to chemokines, R17 interacts with cell-surface GAGs in a process dependent upon two BBXB motifs (where B represents a basic residue) (Lubman et al., 2014). Taken together, our results suggest that R17 plays a role in RHVP immune evasion through targeted sabotage of chemokine-mediated immune surveillance.

To gain insight into the mechanism by which R17 sequesters chemokines, we determined crystal structures alone and bound to CCL3. R17 adopts a two-lobed structure that engages the N-loop region of CCL3 important for recognition by its cognate receptor—a "hotspot" commonly targeted by other pathogen-derived chemokine decoy receptors. A unique element of the R17-CCL3 interaction, however, is the engagement of the 40s-loop BBXB motif that serves an important role in both receptor and GAG binding for a number of pro-inflammatory CC chemokines. Gain-of-function mutational analysis was used to establish that R17 selectively engages this GAG binding determinant of chemokines to form kinetically long-lived complexes. The structure of R17 also revealed an unexpected similarity to the M3 chemokine decoy receptor encoded by MHV-68, although the chemokine binding locations are completely distinct (Alexander et al., 2002).

RESULTS

Structure Determination of RHVP R17

To enable structural studies, recombinant R17 protein was purified from 293F cells cultured with kifunensine, an inhibitor of class I α-mannosidase (Elbein et al., 1991). Before crystallization, R17 was treated with Endoglycosidase H (EndoH) to trim carbohydrate (see Experimental Procedures). The structure of unligated R17 was determined by iodide single-wavelength anomalous dispersion (SAD) with sites located by SHELXD (Sheldrick, 2008), phases estimated using MLPHARE (Dodson et al., 1997), and density modification using PARROT (Cowtan, 2010) (Table 1). The initial model of R17 was built using ARP/wARP (Murshudov et al., 1997), and the final model

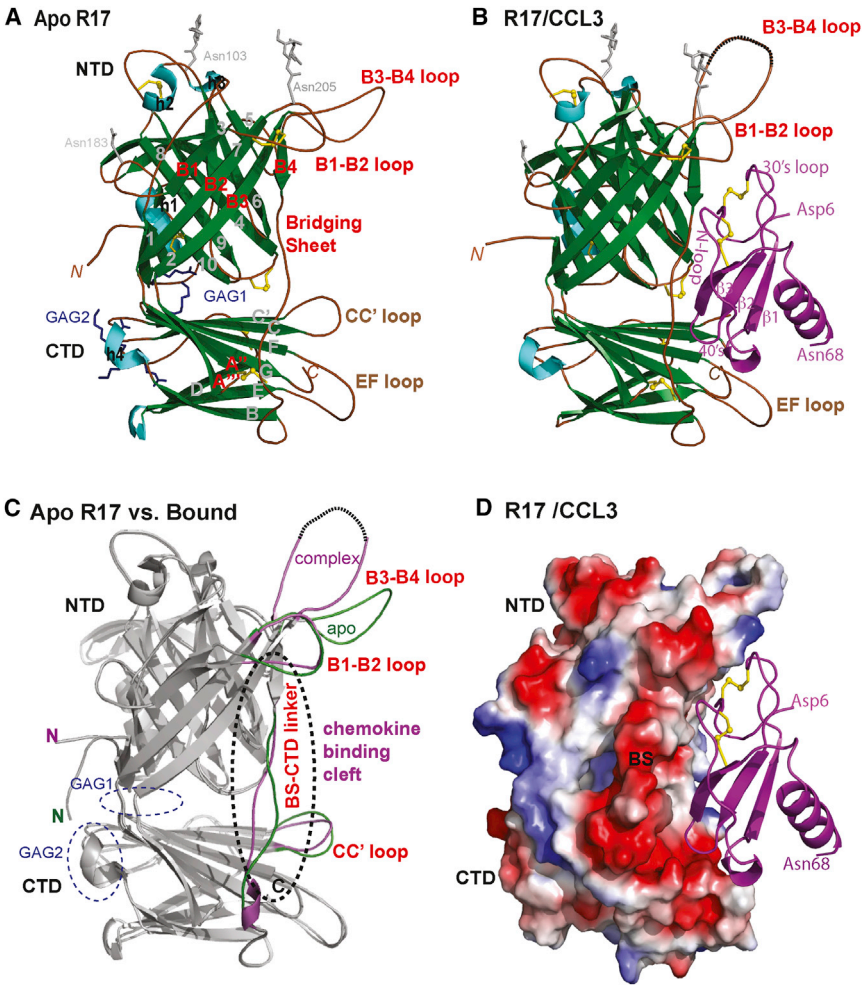

Figure 1. Crystal Structure of RHVP R17 Alone and in Complex with Murine CCL3

(A) Ribbon diagram of apo R17. The N-terminal domain (NTD), bridging sheet (BS), and C-terminal domain (CTD) are colored based on secondary structure: β strands are depicted in green, α helices in cyan, and connecting loops in brown. β strands of the NTD are labeled 1–10, BS is labeled B1–B4, and β strands of the CTD are labeled A–G. During purification, R17 was treated with EndoH to remove complex carbohydrates. Of the three predicted N-linked glycosylation sites, electron density was visible for the N-glycans linked to Asn103 and Asn205. N-Acetylglucosamine (NAG) followed by a mannose ring was built only for Asn205 and is shown in stick representation. Disulfide bonds are shown as sticks and colored yellow.

(B) Crystal structure of the $R17^{GAG2}$ in complex with murine CCL3(D26A) at 3.0 Å resolution. R17 is colored as in (A) while the chemokine is colored magenta and labeled according to accepted chemokine convention. Two NAGs linked to Asn103 and Asn205 are shown in ball-and-stick representation.

(C) Displayed in white cartoon are superimposed free and ligated R17 structures. Conformational changes in the loops around the chemokine binding cleft are colored green (free R17) and magenta (chemokine bound R17). Two GAG binding sites on R17 are located on the opposite surface from chemokine binding and are circled with blue dashed lines.

(D) Electrostatic complementarity between R17 and CCL3. The molecular surface is colored as calculated by APBS (<−1 kT in red, 0 kT in white, and >+1 kT in blue).

See also Figure S1.

was produced after numerous rounds of manual building using Coot (Emsley and Cowtan, 2004) and refinement in Phenix (Adams et al., 2011). The model spans residues 14–400 of the mature protein, with GlcNAc linkages to Asn103 and Asn205 along with 355 water molecules (Table 1 and Figure 1A).

R17 adopts a two-lobed structure with an N-terminal domain (NTD) positioned perpendicular to a C-terminal domain (CTD) linked together by a bridging sheet (BS). The terminal domains consist of β-sandwich folds decorated by loops and helical segments, while the BS is composed of four strands packed with the NTD (residues 190–216 and 233–266) and two strands inserted into the CTD (residues 218–232) (Figure 1A). The NTD spans residues 14–187 and is composed of a seven- and three-stranded sheet (Figure 1A). Three disulfide bonds occur in the NTD; one pins the end of helix h1 to the end of strand s10, one bridges the turn at the start of s4, and another links the end of s4 to the start of s9. The CTD spans residues 285–400 and adopts an approximately I-type immunoglobulin fold composed of nine β strands and a disulfide linking the C′ strand with the beginning of the D strand. A long flexible linker connects the BS and CTD, specifically residues 265–288, of which residues 267–270 are refined with high *B* factors. One disulfide is found within the BS B1-B2 loop while another joins the end of the flexible BS linker to the A″ strand inserted into the CTD.

Structural Relatives of R17

We looked for proteins of related structure to R17 using the Dali server (Holm and Sander, 1995), and remarkably found that the two closest relatives are both from gammaherpesviruses: M3 encoded by MHV-68 (*Z* score = 14.1) and GP350 encoded by Epstein-Barr virus (EBV) (*Z* score = 8.2). The structures of R17 and M3 aligned with a root-mean-square deviation (rmsd) of 4.2 Å over 262 residues including five disulfide bonds, despite displaying only 8% sequence identity (Figures 2A and 2B). While similarities with both terminal domains are readily apparent, the NTDs of R17 and M3 align best (rmsd = 3.3 Å for aligned 150 residues with 11% sequence identity). The R17 BS architecture between the NTD and CTD is absent in M3, which instead has a series of large helical loops that decorate the CTD.

The core of the R17 CTD domain also displays structural similarity to the second immunoglobulin (Ig) domain of the viral surface glycoprotein GP350 encoded by EBV (rmsd of 2.8 Å for 109 aligned residues, with 9% sequence identity). EBV infects B cells through binding of GP350 to complement receptor 2 (CR2) (Nemerow et al., 1987) using residues from the N-terminal Ig

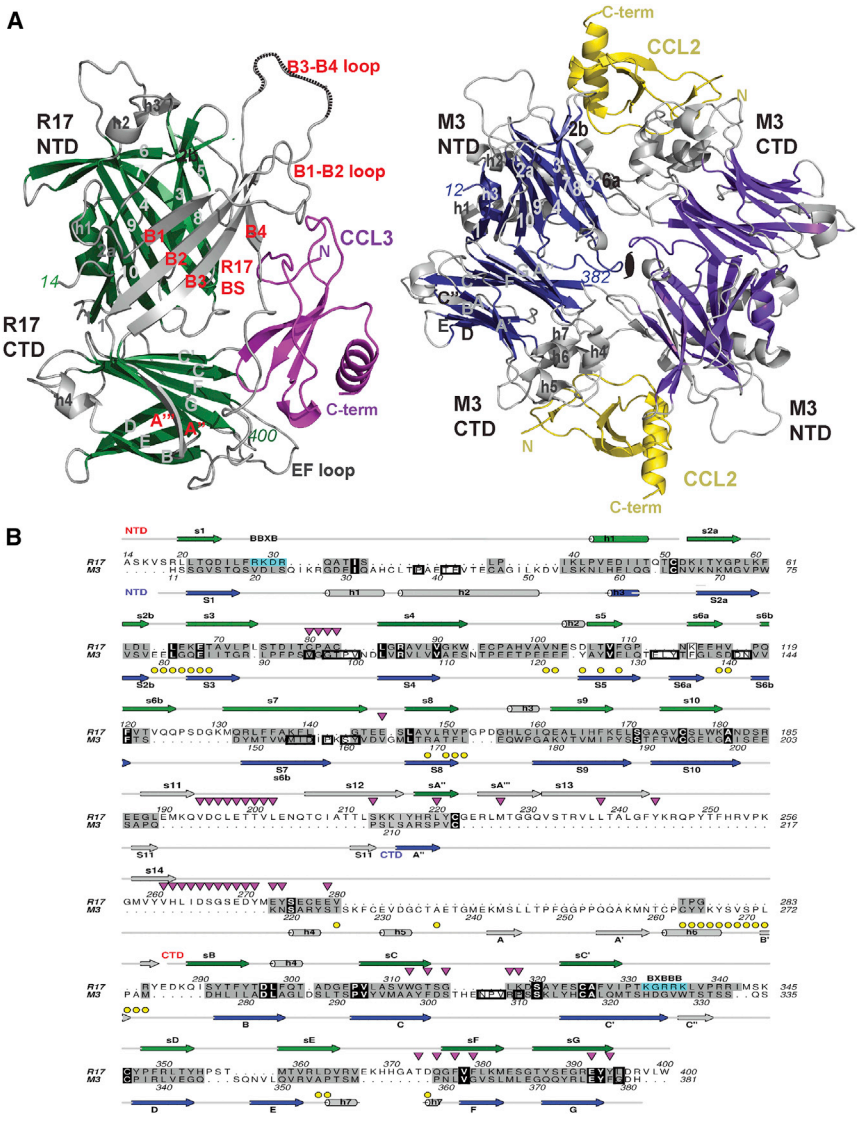

Figure 2. Structural Comparison of R17 with M3

(A) Comparison of CCL3 (magenta) bound R17 with CCL2 (yellow) bound M3 where shared core secondary structure elements are depicted in green for R17 and dark blue for M3. Divergent structural elements are depicted in light gray in both R17 and M3.

(B) Structure-based sequence alignment of R17 with M3. Secondary structure elements of R17 are on top while secondary structure elements of M3 are on the bottom. Both are colored as in Figure 1A. Structurally similar residues are colored gray, while identical residues are in black. Yellow circles denote M3 chemokine binding interface residues, while down-pointing magenta triangles denote R17 chemokine binding interface residues. Residues buried in the M3 dimer are boxed. BBXB motifs on R17 are boxed in cyan.

See also Figure S2.

domain and the linker connecting the first Ig to the second (Szakonyi et al., 2006). We tested the ability of biotinylated R17 to bind CR2-positive B cells in wild-type versus CR2 knockout mice (Molina et al., 1996; Wu et al., 2000). No differences in cell staining were noted (data not shown).

Mutational Analysis Based on M3 Chemokine Binding Determinants

We attempted to define the chemokine binding site on R17 based on the structural similarity to M3 (Figure S1A) (Alexander et al., 2002). As opposed to monomeric R17, M3 is an anti-parallel homodimer with deep chemokine binding clefts formed between the NTD and CTD of the opposing monomers. We reasoned that the loop connecting strands 2b to 3 of R17 is structurally equivalent to the chemokine binding loop s2b-3 from the NTD of M3. By the same token, the large loop connecting strands B3 to B4 in the BS of R17 could mimic the chemokine binding region in the CTD of M3 (Figure S1A, dotted circles). To experimentally address our hypothesis, we constructed two R17 variants: $R17^{65AAAA68}$ has residues ^{65}LEKE^{68} of the s2b-3 loop mutated to Ala and $R17\Delta^{248-254}$ has residues 248 through 254 of the B3-B4 loop deleted. To our surprise, neither of the R17 variants had altered binding to two chemokines we tested, CCL2 and CCL3 (Lubman et al., 2014) (Figure S1B), indicating that ligand engagement is most likely localized elsewhere on the protein.

Crystal Structure of the R17-CCL3 Complex

To address where chemokines bind R17 we initiated co-crystallization experiments with CCL3, a chemokine we previously had shown binds the decoy receptor with an exceptionally long kinetic half-life leading to the potent inhibition of PBMC transmigration (Lubman et al., 2014). Diffraction quality crystals were obtained using a CCL3 mutant (D26A) reported to reduce aggregation (Czaplewski et al., 1999) and an $R17^{GAG2}$ variant that could no longer interact with cell surfaces due to the mutation of residues ^{333}KGRRK^{337} to ^{333}DGEED^{337}. The structure of the complex was solved by molecular replacement with a final atomic model refined to 3.0 Å resolution (Table 1 and Figure 1B). Each asymmetric unit contained two $R17^{GAG2}$-CCL3 complexes, with two GlcNAc linkages to Asn103 and Asn205 of R17 in chain A and a single GlcNAc linkage to Asn205 built for chain B. Using multi-angle static light scattering we determined that R17 binds CCL3 with 1:1 stoichiometry, suggesting that additional lattice interactions observed in the crystal structure are not functionally relevant (Figure S2).

The primary structural element used by R17 to create a chemokine binding platform is the flexible linker that connects the BS of R17 with the CTD and forms a hydrophobic cavity between the two β sandwiches. While this region is not well

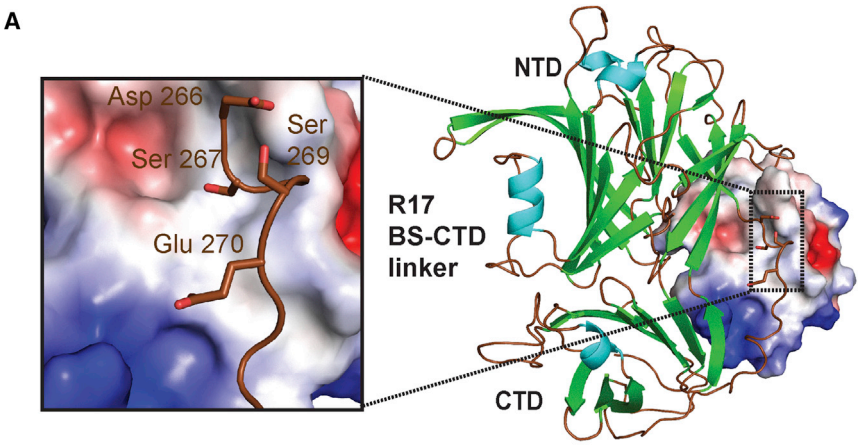

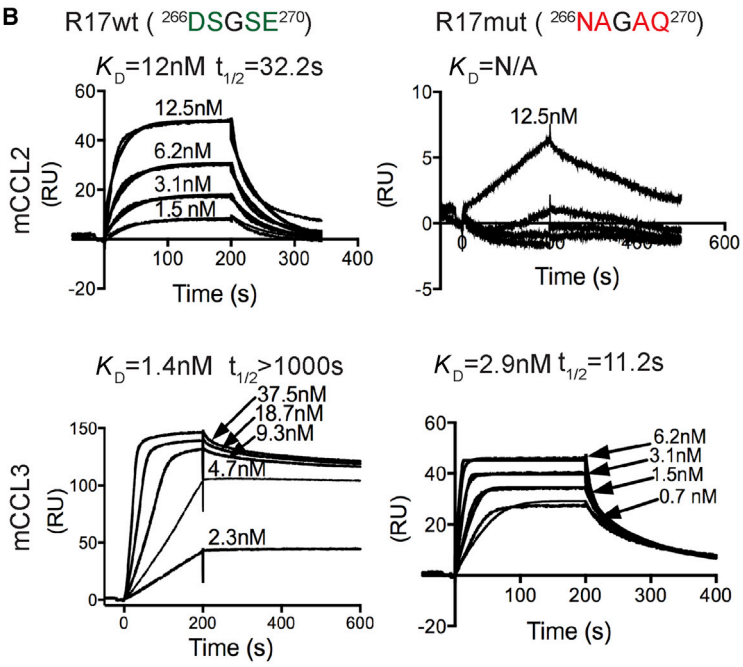

Figure 3. Experimental Assessment of Crystallographic Observations

(A) Structure of the R17-CCL3 complex where chemokine is in electrostatic surface representation. Inset shows a part of the linker region connecting BS and CTD domains. Residues ^{266}DSGSE^{270} were mutated ^{266}NAGAQ^{270}.

(B) SPR analysis of mCCL2 and mCCL3 binding to the R17 ^{266}NAGAQ^{270} mutant immobilized to a CM5 chip. Shown are response curves for a typical chemokine titration. The experimental curves were globally fit using a 1:1 mass transport model to determine the kinetic K_D and half-life ($t_{1/2}$) presented above each sensorgram. Values for K_D are means of three independent experiments where $K_D = k_d/k_a$ and $t_{1/2} = 0.693/k_d$. wt, wild-type; mut, mutant.

ordered in the crystal structure of the unligated R17, it becomes partially ordered upon ligand binding (Figure 1C). There are 31 residues from CCL3 and 46 residues from R17 at the R17-CCL3 interface, leading to 2,700 Å^2 of buried solvent-accessible surface area (1,385 Å^2 buried for CCL3 and 1,298 Å^2 buried for R17). The shape complementarity at the R17-CCL3 interface is calculated to be Sc = 0.70 (Lawrence and Colman, 1993). In addition to the linker that connects the two domains, CCL3 is "clamped" through multiple interactions with both the BS and CTD. A primary structural element of the BS used to bind chemokines is the B1-B2 loop. A notable hydrophobic pocket is formed by R17 residues Val195, Leu198, Leu239, and Leu264, which serves to sequester CCL3 Phe13, a critical residue for GPCR binding (Laurence et al., 2000). The hydrogen bonds observed between the main chain carbonyl oxygens of Glu199 and Thr200 in R17 with Ser35 of CCL3 serve as yet another anchor to the BS of R17. Another pocket buries Arg45 and Asn46 of the CCL3 40s-loop BBXB motif, formed mainly by R17 residues Tyr272, Tyr275, Trp313, Phe378, and Tyr395. Within this acidic pocket a prominent salt bridge is formed between Glu393 of R17 and Arg45 of CCL3. Arg45 is the first B (basic residue) of the BBXB GAG binding motif on CCL3, and was shown to be critical for the ability of CCL3 to bind heparin sulfate and the CCR5 receptor (Kim et al., 2001; Koopmann et al., 1999; Teng et al., 2008).

Comparison of apo with chemokine bound R17 points to several conformational variations associated with ligand binding (Figure 1C). Significant conformational differences are observed in the linker region connecting the BS and CTD that makes numerous chemokine contacts. Large conformational differences are also observed in the B1-B2 loop, B3-B4 loop, and CC′ loop of the CTD, each of which flank the engaged chemokine (Figure 1C). The fact that R17 uses structurally labile elements to engage chemokines suggests that structural plasticity may be associated with its broad ligand binding specificity.

Mutational Analysis of the R17 Chemokine Recognition Site

To experimentally assess our crystallographic observations, we mutagenized the linker region of R17 and selectively removed the negative charge from ^{266}DSGSE^{270} to ^{266}NAGAQ^{270}. The resulting R17 variant could no longer bind to CCL2 (concentration range tested up to 150 nM) and bound to CCL3 with more than 100-fold ($t_{1/2}$ = 11 s) faster kinetic off-rate compared with wild-type R17-CCL3 interactions (Figure 3). Thus, the deleterious effects of the linker mutations are more pronounced for R17-CCL2 interactions. This mutational analysis of R17 establishes that our structurally defined recognition site for CCL3 is

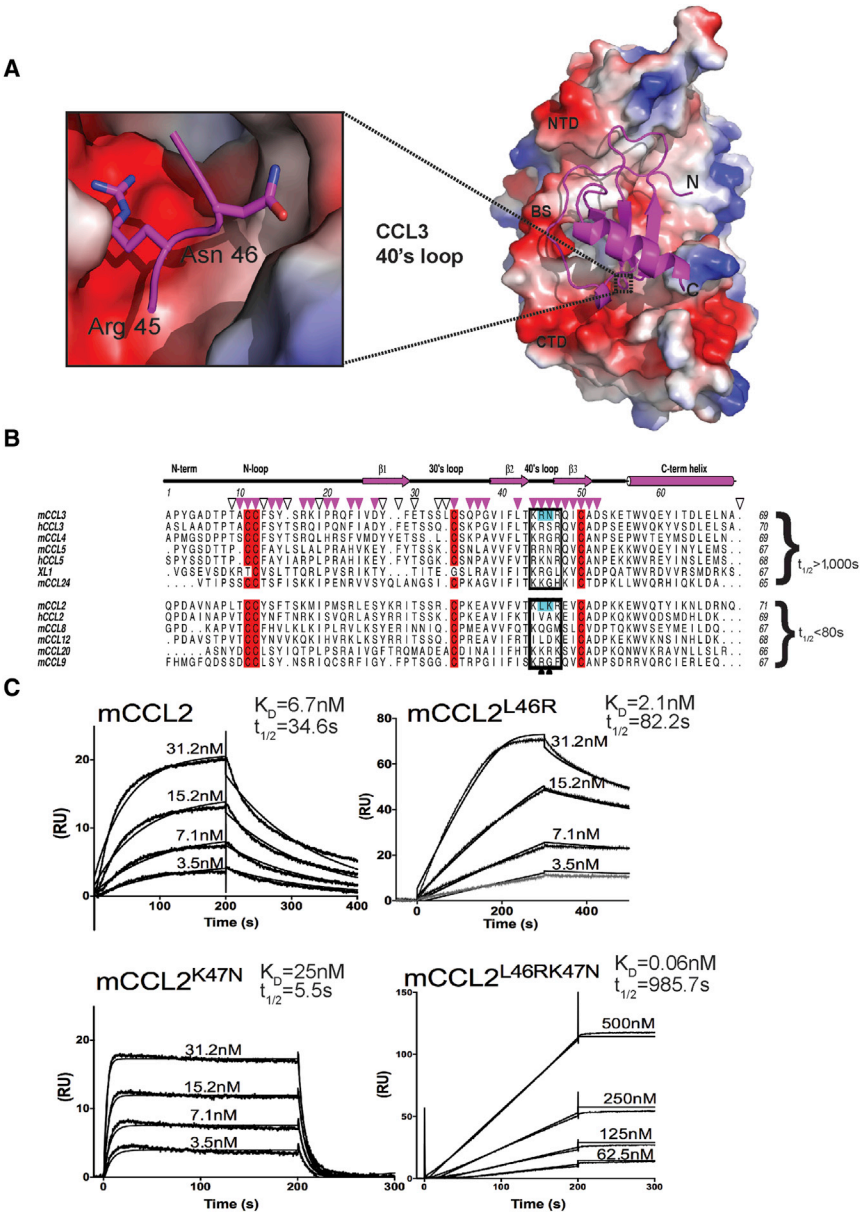

Figure 4. Analysis of Chemokine Binding Kinetics

(A) Structure of the R17-CCL3 complex where R17 is in electrostatic surface representation. The inset shows how Arg45 and Gln46 of CCL3 are buried into a surface pocket of mixed acidic and hydrophobic character. A prominent salt bridge is observed between Arg45 of CCL3 and R17 Glu393, while the side chain of Asn46 makes a hydrogen bond with the hydroxyl of R17 Tyr323.

(B) Structure-based sequence alignment of CC chemokines known to interact with R17 ordered of according to the kinetic stability (as measured by $t_{1/2}$) of the complex they form. Conserved cysteines are colored red; residues of the BBXB motif in the 40s-loop are boxed; residues of CCL2 mutated to structurally equivalent residues in CCL3 are colored cyan. Down-pointing magenta triangles denote CCL3 side chains beyond Cα that make direct contact (<4 Å) with R17 and are conserved in both R17-CCL3 complexes in the asymmetric unit of the crystal. Additional residues that lose any solvent-accessible surface area in either complex are marked with open black triangles. Note that the recombinant CCL3 protein used for co-crystallization has D26A mutation.

(C) SPR curves showing the effect of chemokine mutations on binding to $R17^{GAG2}$ coupled CM5 chip: wild-type mCCL2 (left), $mCCL2^{L46R}$ (right), $mCCL2^{K47N}$ (bottom left), and $mCCL2^{L46R\ K47N}$ mutant (bottom right). The experimental curves were globally fit using a 1:1 mass transport model to determine the kinetic K_D and half-life ($t_{1/2}$) presented above each sensorgram. Values for K_D are means of three independent experiments where $K_D = k_d/k_a$ and $t_{1/2} = 0.693/k_d$.

shared by CCL2 and, likely, the additional CC and C chemokines it binds.

R17 Binds Chemokines and Cell-Surface GAGs at Two Distinct Sites

We previously reported that R17 contains two BBXB motifs located at distal ends of its linear sequence that allow it to interact with cell surfaces (Lubman et al., 2014). We hypothesized that cell-surface binding will permit R17 to sequester chemokines locally, perhaps at the site of infection. Charge reversal of either one of these motifs abrogated the ability of R17 to bind to the surface of Chinese hamster ovary (CHO) cells but did not compromise its ability to interact with chemokines (Lubman et al., 2014). The crystal structure of R17 supports our initial observations and provides insight as to how GAG binding by R17 is accomplished. Despite being far apart in the linear sequence, the two BBXB motifs found on R17 are in physical proximity to one another, coming together to create a large positively charged surface patch at the junction of the NTD and CTD (Figure 1C). These GAG binding determinants are located more than 40 Å away from the chemokine binding site on the opposite face of R17 (Figure 1D). Interestingly, no basic clusters are located on the surface of M3 (Figure 2B). Mechanistically, these findings are in agreement that R17, but not M3, can bind cell surfaces while simultaneously interacting with chemokines (Lubman et al., 2014).

Kinetically Stable R17 Interactions Are Imparted by Chemokine 40s-Loop Residues

Kinetic analysis of R17 binding to different chemokines identified two types of R17-chemokine interactions. Kinetically stable complexes were formed with CCL3, CCL4, CCL5, CCL24, and XCL1 ($t_{1/2}$ > 1000 s), while significantly faster off rates were observed for the binding of CCL2, CCL8, CCL9, and CCL20 (Lubman et al., 2014). To address the structural basis for these distinct kinetic off rates, we undertook a comparative analysis of R17 binding chemokines in the context of our R17-CCL3 structure (Figure 4A). The alignment of characterized

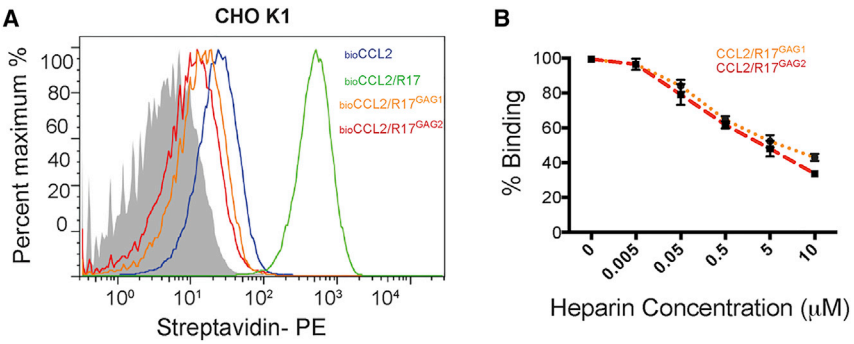

Figure 5. R17 Inhibits CCL2 Interaction with Cell-Surface GAGs

(A) FACS analysis monitoring the effect of wild-type R17, $R17^{GAG1}$, and $R17^{GAG2}$ on the interaction of CCL2 with cell-surface GAGs as measured by changes in mean florescence intensity. 50 nM biotinylated CCL2 was added to CHOK1 cells in the presence or absence of 100 nM $R17^{GAG1}$ (orange line), 100 nM $R17^{GAG2}$ (red line) or 100 nM wild-type R17 (blue line). Cell-surface bound CCL2 was detected with streptavidin PE using FACSCalibur (BD Biosciences) and data were analyzed with FlowJo. Representative histogram plot shows inhibition of CCL2-GAG interactions by $R17^{GAG1}$ and $R17^{GAG2}$.

(B) R17 competes with soluble heparin sulfate for chemokine binding. $R17^{GAG1}$ and $R17^{GAG2}$ were immobilized to a CM5 chip and mCCL2 was injected at a concentration of 100 nM, alone or in combination with the indicated increasing concentrations of heparin sulfate (0, 50 nM, 500 nM, 1 μM, 5 μM, and 10 μM). Error bars represent the SE of three independent experiments.

chemokines suggested to us that kinetic stability of the R17-CCL3 complex might be regulated by basic residues in the chemokine 40s loop. If true, replacement of structurally equivalent residues in CCL2 with residues found in CCL3's 40s loop could extend the kinetic half-life of the R17-CCL2 complex. To test our hypothesis, we created a $CCL2^{L46RK47N}$ variant (Figure 4B) and evaluated its binding to an R17-coated CM5 chip (Figure 4C, bottom right). The surface plasmon resonance (SPR) binding profile of the $CCL2^{L46RK47N}$ double mutant resembled that of CCL3, characterized by an apparently slow kinetic on-rate and a half-life exceeding 15 min (Lubman et al., 2014). To further dissect the contribution of individual 40s-loop residues to complex stability, we created two additional CCL2 variants: $CCL2^{L46R}$ and $CCL2^{K47N}$. We found that the $CCL2^{L46R}$ variant has a 2-fold longer half-life compared with the wild-type CCL2-R17 interaction (Figure 4C, top right), while the $CCL2^{K47N}$ mutant forms a less stable complex with a $t_{1/2}$ of only 5.5 s (Figure 4C, bottom left). Thus, the single-site mutations only partially explain the binding profile of the $CCL2^{L46RK47N}$ variant, which could be stabilized by energetic coupling at the 40s-loop binding interface (Lubman and Waksman, 2002).

R17 Can Inhibit Chemokine-GAG Interactions

We next sought to address the question of whether CCL2, whose GAG binding site is localized outside of the BBXB motif in the 40s loop, loses its ability to interact with GAGs when bound to R17. The addition of wild-type R17 results in a dramatic increase in CCL2 staining of CHO cells due to the decoy receptor's ability to bind cell-surface GAGs and chemokines simultaneously (Figure 5A) (Lubman et al., 2014). We therefore mutated the two GAG binding sites on R17 and examined whether our $R17^{GAG1}$ and $R17^{GAG2}$ variants (Lubman et al., 2014) were capable of disrupting the binding of biotinylated CCL2 to CHO cells (Figure 5). The addition of either GAG binding null R17 variant resulted in significantly decreased CCL2 staining. To further examine this issue, we designed an SPR-based competition experiment whereby a fixed concentration of CCL2 was complexed with varying amounts of heparin sulfate and flown over immobilized $R17^{GAG1}$ or $R17^{GAG2}$. We found that addition of heparin sulfate to 100 nM of CCL2 blocked $R17^{GAG1}$ and $R17^{GAG2}$ interactions in a concentration-dependent manner, with 50% of binding disrupted using 50-fold excess of heparin sulfate. Together these experiments indicate that R17 is capable of disrupting direct chemokine-GAG interactions for chemokines such as CCL2 that employ determinants outside the 40s loop.

DISCUSSION

Parallel Evolution of the R17 and M3 Chemokine Decoy Receptors

With less than 8% sequence identity, the crystal structure of the unligated R17 revealed unexpected structural similarity to MHV-68 encoded M3 (Figure 2A). We thus proceeded to use the crystal structures of M3 bound to CCL2 and XL1 (Alexander et al., 2002; Alexander-Brett and Fremont, 2007) to assess the chemokine binding site of R17. Two R17 variants were designed and tested based on structurally equivalent chemokine binding regions in M3, neither of which exhibited perturbed binding to CCL2 or CCL3 (Figure S1B). We therefore determined the crystal structure of R17 bound to CCL3, which revealed that the spatial location of chemokine binding on R17 is completely distinct from that of M3. In contrast to M3, where two chemokine binding clefts are formed at the distal ends of an anti-parallel homodimer, R17 engages chemokines as a monomer primarily using a BS that is completely absent from M3 and, likely, the related M1 and M4 proteins encoded by MHV-68 as well (Alexander et al., 2002; Clambey et al., 2000; Evans et al., 2006; O'Flaherty et al., 2014). Interestingly, the R17 chemokine binding cleft is located in a structurally analogous position as the M3 dimer interface (Figure 2). Thus, despite a shared structural scaffold, the capacity of these two herpesvirus proteins to disrupt chemokine function appears to have arisen independently. Nevertheless, the chemistry of each chemokine binding niche is similar, with primarily hydrophobic residues packing against the chemokine N loop and acidic residues poised to engage basic chemokine regions.

Unifying Feature of Chemokine Recognition

Pathogens often employ a general strategy of molecular mimicry to subvert host defense. To understand how unrelated proteins encoded by distinct pathogens disrupt chemokine signaling, we compared the recently solved crystal structures of vMIP-II/CXCR4 and CX3CL1/US28 (Burg et al., 2015; Qin et al., 2015)

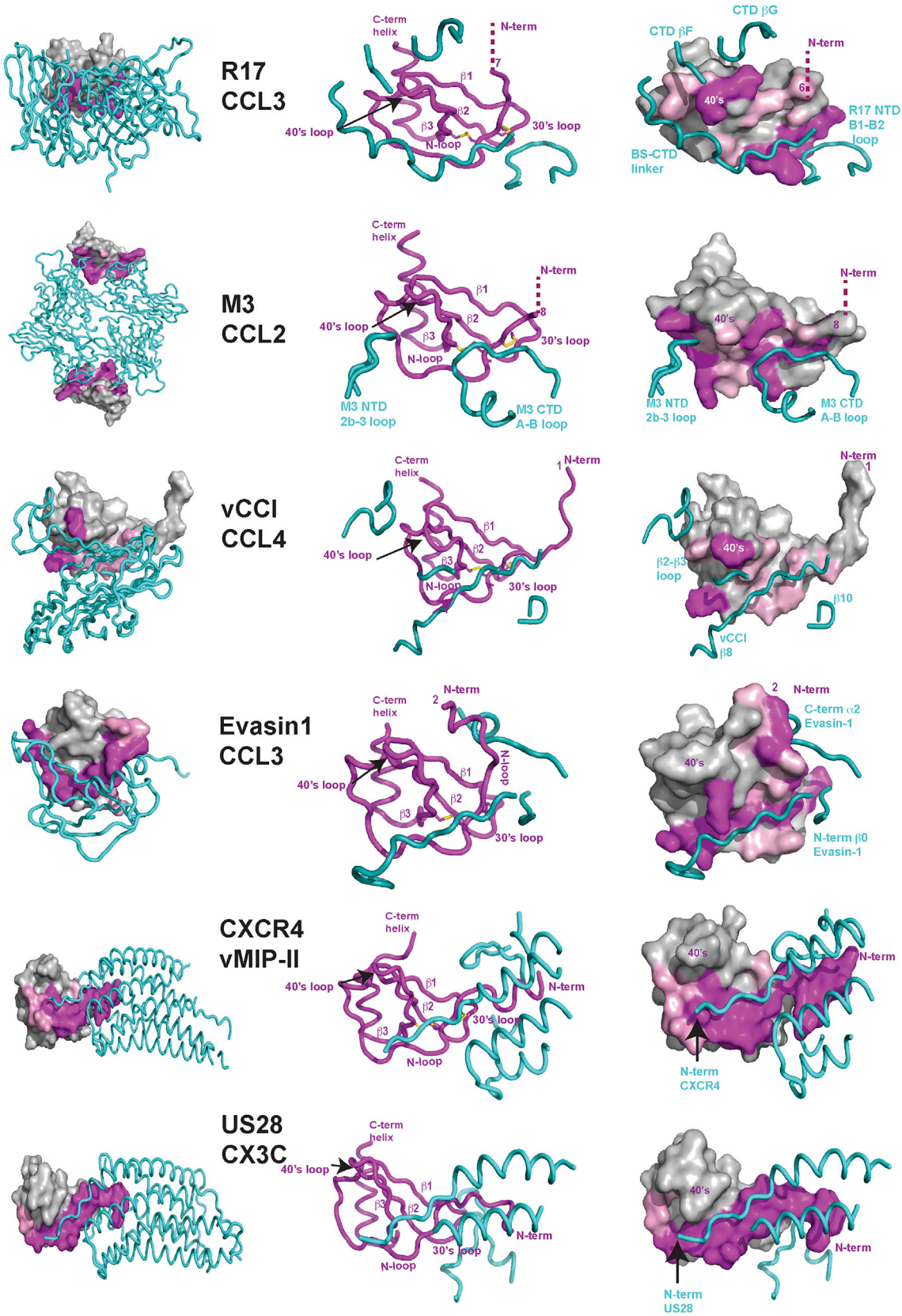

(legend on next page)

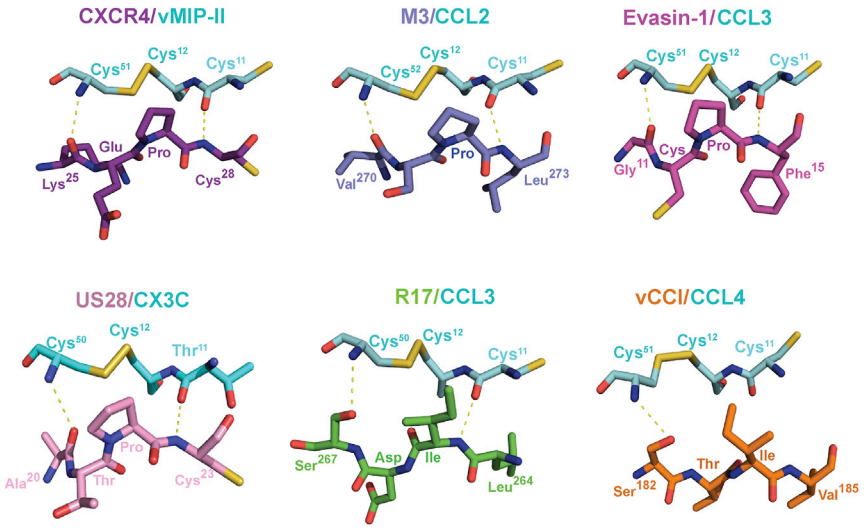

Figure 7. Conserved Recognition of Chemokine Invariant Disulfide

The invariant disulfide bond (Cys^{12}-$Cys^{50/51/52}$) and flanking Cys^{11} of different chemokines are depicted in ball-and-stick representation with carbon colored cyan, nitrogen blue, oxygen red, and sulfur yellow. Decoy and signaling receptor residues that engage the chemokine invariant disulfide are depicted with carbon green for R17 (PDB: 4ZLT), light blue for M3 (PDB: 2NZ1), orange for vCCI (PDB: 2FFK), magenta for Evasin-1 (PDB: 3FPT), purple for CXCR4 (PDB: 4RWS), and pink for US28 (PDB: 4XT3). Conserved hydrogen bonds made with chemokine main chain atoms flanking the invariant disulfide are represented by dotted yellow lines.

with CC chemokines bound to poxvirus vCCI (Zhang et al., 2006), tick Evasin-1 (Dias et al., 2009), herpesvirus M3 (Alexander et al., 2002; Alexander-Brett and Fremont, 2007), and R17 (Figure 6). This comparative analysis of chemokine signaling and secreted decoy receptors revealed one universal aspect of recognition: the targeting of the invariant disulfide found in all four chemokine classes. Indeed, a similar chemical strategy is used by each chemokine binding protein to engage the disulfide bridge and flanking main chain. CXCR4, US28, M3, and Evasin-1 all use a Pro residue to contact the disulfide while R17 and vCCI employ Ile. The backbone conformation surrounding the invariant disulfide is also highly conserved in these structures, where the main chain carbonyl of Cys11 serves as hydrogen bond acceptor and the amide of Cys50, Cys51, or Cys52 serves as a hydrogen bond donor. In addition, all of the receptors employ an extended β strand to make these contacts, with all but R17 oriented in an anti-parallel configuration. Thus, it appears that many pathogen-encoded chemokine decoys mimic precisely the same structural and chemical environment as GPCRs to engage chemokines. Since the invariant disulfide is present in all four chemokine classes, this unifying aspect of chemokine recognition could potentially be exploited for the design of small-molecule inhibitors.

Promiscuous versus Chaste Chemokine Engagement

The chemokine signaling network employs approximately 50 chemokines and 20 GPCRs, with chemokines activating a select few receptors in a class-specific fashion. In contrast, many of the characterized pathogen-encoded decoy receptors bind a broad spectrum of different chemokines from multiple chemokine families. For example, M3 is able to bind chemokines from all four classes (van Berkel et al., 2000), R17 interacts with the CC and C family of chemokines, and vCCI broadly recognizes CC and some CXC chemokines (Graham et al., 1997). The exceptions include the tick Evasins (Deruaz et al., 2008; Frauenschuh et al., 2007) and HCMV-encoded pU21.5 (Wang et al., 2004) that exhibit chemokine-selective binding profiles. Structural comparison of four pathogen-encoded chemokine decoys reveals that while they all extensively engage the chemokine N loop, only Evasin-1 engages the N term of CCL3 (Figure 7). Consistent with this observation, the N termini of chemokines are thought to be responsible for specific receptor activation (Clark-Lewis et al., 1995). Indeed, truncations or mutations in the N termini of chemokines generally lead to a loss in agonist activity, although receptor binding affinity can be maintained (Pease et al., 1998). Thus, it appears that R17 along with M3 and vCCI achieve promiscuity by making extensive interactions with the invariant disulfide and N-loop regions of chemokines, while the N-term region important for chemokine receptor specificity is ignored. On the other hand, Evasin-1 exclusively interacts with CCL3 and CCL4 perhaps by virtue of extensive N-term engagement (Dias et al., 2009), a trait shared by GPCR chemokine receptors (Burg et al., 2015; Qin et al., 2015).

Roles of GAG Binding Determinants

R17 broadly binds CC and C chemokines with nanomolar affinities, but SPR studies indicate that only a subset (CCL3, CCL4, CCL5, CCL24, and XCL1) form kinetically stable complexes with apparent half-lives exceeding 1 hr (Lubman et al., 2014). While these chemokines serve to recruit a wide array of immune cells during viral infection, what they share in common is a GAG binding BBXB motif in their 40s loop. To examine the role of these residues in R17 binding we created a CCL2 variant with the same BBXB motif as found in the 40s loop of CCL3 (KRNR). Strikingly, the mutant CCL2 was endowed with an extremely long half-life when bound to R17. Thus, R17 appears

Figure 6. Comparison of the Chemokine Binding by Four Pathogen-Derived and Two Host Receptors

Structures of R17 (PDB: 4ZLT), M3 (PDB: 2NZ1), vCCI (PDB: 2FFK), Evasin-1 (PDB: 3FPT), CXCR4 (PDB: 4RWS), and US28 (PDB: 4XT3) in complex with different chemokines were superimposed with all chemokines displayed in the same orientation. Displayed at far left are chemokine bound complexes where pathogen-derived decoys and GPCRs are shown in worm diagram while chemokines are shown in surface representation. Depicted in the middle are worm diagrams of the complexes highlighting the chemokine fold and receptor contact regions. Diagrams on the right are shown to highlight chemokine surface regions engaged by individual receptor determinants. Chemokine residues making direct contact (<4.0 Å) are labeled in magenta. Additional interfacial residues that lose solvent-accessible surface area in the complex are colored pink.

to target chemokine 40s-loop BBXB motifs to drive extremely stable complex formation.

Studies of MHV-68-encoded M3 indicate that it potently disrupts chemokine-GAG interactions, and thereby decoy receptor complexes are likely trafficked away from infected cells (Alexander-Brett and Fremont, 2007). A unique functional element of R17 is the capacity to engage cell-surface GAGs using two of its own BBXB motifs positioned distal from the chemokine binding site. There are no similar basic patches on the surface of M3, and no functional evidence of M3 cell-surface interactions has been reported. R17 is most likely positioned in the local extracellular matrix during infection where it can sequester inflammatory chemokines, rendering them inactive. We anticipate that fluid-phase chemokines would readily bind R17, while GAG associated chemokines, such as CCL2, would likely need to dissociate before R17 engagement. This unique functional attribute of R17 provides a distinct immune evasion strategy that may find therapeutic application in cases where localized disruption of chemokine signaling networks is preferred over systemic disruption, such as allograft rejection (Proudfoot et al., 2015).

Conclusions

A recurrent theme among pathogens is the repurposing of structural scaffoldings to facilitate the evasion of host immune defense. For example, viruses use the major histocompatibility complex (MHC) fold to engage natural killer (NK) cell receptors to protect infected cells from NK cell-mediated cytotoxicity (Krmpotic et al., 2005). Still other viruses employ the MHC fold to, for example, prevent NKG2D ligand-surface expression or competitively block tumor necrosis factor ligand-receptor interactions (Lodoen et al., 2004; Wang et al., 2012; Zhi et al., 2010). Thus, it is not particularly surprising that RHVP employs a protein of similar structure as MHV-68 M3 to block chemokine signaling networks. What is surprising, however, is that R17 has in parallel developed the capacity to sequester chemokines using determinants completely distinct from those employed by M3.

EXPERIMENTAL PROCEDURES

Mammalian Production of RHVP R17 and R17^{GAG2}

The cloning, expression, and purification of wild-type R17 and its variants has been described in Lubman et al. (2014). For crystallization, we employed an alternative version of the published protocol developed to minimize the amount of N-linked carbohydrate (Chang et al., 2007). This involved expression of both R17 and R17^{GAG2} mutant in medium containing 1 mM of the glycosylation processing inhibitor kifunensine. The culture medium was collected 10 days after transfection and was purified using Ni-agarose beads (Qiagen). The eluted protein was buffer exchanged into 50 mM HEPES (pH 7.5) and 600 mM NaCl, and incubated at room temperature overnight with EndoHf (3000 U of EndoH for 1 μg of protein) (New England Biolabs). The digested material was passed over an amylose column to remove the EndoHf/maltose-binding protein fusion, followed by size-exclusion chromatography (SEC) on a HiLoaD 26/60 Superdex 200pg column (GE Healthcare). For purification of the wild-type R17, the NaCl concentration was maintained at 600 mM throughout purification and crystallization. For the R17^{GAG2} variant, the NaCl concentration was maintained at 150 mM for subsequent co-purification with CCL3 (see below).

Escherichia coli Production of Murine CCL3(D26A)

The gene encoding the mature form of murine CCL3 with optimization for *E. coli* codon usage was cloned into a pET28A vector (Novogen, EMD Biosciences) using NheI and BamHI restriction sites. The D26A mutant was generated by site-directed mutagenesis (Agilent Biotechnologies). The CCL3(D26A) mutant was expressed in *E. coli* BL21(DE3) cells, and protein production was induced using 1 mM isopropyl β-D-1-thiogalactopyranoside. CCL3(D26A) partitioned into the inclusion body fraction and was refolded using the arginine oxidative refolding method (Nelson et al., 2014). In brief, a 400-ml volume of arginine refolding buffer (400 mM L-arginine, 100 mM Tris [pH 8.5], 5 mM reduced glutathione, 0.5 mM oxidized glutathione, and 0.2 mM PMSF) was prepared. Into this buffer, four injections of 500 μl of solubilized inclusion body were made over the course of 2 hr (0, 30 min, 60 min, and 120 min). The refolding buffer was then allowed to stir slowly overnight at 4°C. The following day the protein was filtered, concentrated using a YM-10 (10-kDa cutoff) filter membrane (Millipore) to a volume of 2 ml, and purified with SEC using a High Load 16/60 Superdex S75 prep grade column (GE Healthcare).

Crystallization and Structure Determination of R17

R17 was prepared for crystallization by SEC purification in buffer containing 25 mM HEPES (pH 7.5), 600 mM NaCl, and 0.01% Na azide. R17 was then concentrated to 22 mg/ml and used to set up crystallization trials by hanging-drop vapor diffusion. Crystals of R17 were obtained in 18%–25% polyethylene glycol (PEG) 550MME and 100 mM Tris-HCl (pH 8.5) in space group $P2_12_12_1$ (a = 69.561 Å, b = 75.835 Å, c = 106.985 Å) with one molecule in the asymmetric unit. Crystals were soaked for up to 5 min into a solution similar to the precipitant solution, but supplemented with 25–250 mM of KI. Diffraction data for several iodide derivatives were collected at the Advanced Light Source (ALS) beamline 4.2.2 (Lawrence Berkeley Laboratories) at a wavelength of 1.77 Å (iodide edge) at 100 K with a CCD detector. 360° of data were collected for all datasets to maximize the multiplicity of the data (Cianci et al., 2008; Yogavel et al., 2007, 2009), which lowered the error in the measurement of Bijvoet pairs and thereby increased the accuracy of the anomalous signal (Schneider and Sheldrick, 2002). Individual iodide derivative datasets were processed, indexed, and scaled using HKL3000 (Minor et al., 2006). Anomalous signal from individual datasets was not sufficient for successful structure determination. However, merging of two iodide derivative datasets with the ratio of anomalous signal defined at 0.2 allowed SHELDX to find 14 iodide sites, and subsequent SAD phase calculation led to interpretable experimental electron density maps. ARP/wARP was used to trace over 85% of the model into experimental density and an initial 2.7-Å model was refined to R_{work} = 37.16% and R_{free} = 46.01%. The 2.7-Å model was used as a search model for molecular replacement of the 1.9-Å native dataset collected at Advanced Photon Source (APS) beamline 23-ID-D. After several rounds of manual model building using Coot, Phenix (Adams et al., 2011) was used to refine the R17 structure to a final R_{work} of 18.4% and R_{free} of 22.08%. The final R17 model contains mature residues 14–400, two Asn-GlcNAc linkages, and 355 water molecules.

Crystallization and Structure Determination of the R17^{GAG2}/CCL3 Complex

The mouse CCL3 variant (D26A) was produced in *E. coli* and harbors the mutation D26A. The purification of the R17^{GAG2} variant is described in the previous section. The two proteins were mixed in a 1:5 molar ratio of R17 to CCL3. The 1:1 complex was purified using SEC on the HiLoaD 26/60 Superdex 200pg column (GE Healthcare). Crystals of the R17^{GAG2}/CCL3 complex at 60 mg/ml were grown using 22% PEG 3350 and 0.4 M Mg nitrate. Crystals of the complex belong to the I222 space group, with two molecules of R17^{GAG2} and two molecules of CCL3(D26A) in the asymmetric unit. Native data were collected at the ALS beamline 4.2.2 (Lawrence Berkeley Laboratories) at a wavelength of 1 Å at 100 K with a CCD detector. The structure of R17 alone and human CCL3 (PDB: 2X69) was used to solve the structure of the complex by molecular replacement using Phaser within Phenix (Adams et al., 2011). The final model has an R value of 21.52% and R_{free} of 27.40%. The refined atomic model of R17^{GAG2}/CCL3(D26A) comprises residues 18–400 chain A/chain B of R17 and residues 7–68 chain D/chain E of CCL3 along with two N-linked glycosylation sites for each R17 chain. Due to poor electron density, residues 249–254 of chain A and 247–254 of chain B were not included in the final model. All of the structural analyses described were done on AD complex.

Flow Cytometry

To evaluate the effect of R17 and its variants on the ability of CCL2 to interact with cell surfaces, chemokines and a negative control protein (MR1)

were non-specifically biotinylated using an EZ-biotin kit (Pierce) with a 2:1 biotin to protein molar ratio, followed by removal of unbound biotin (Thermo Scientific Zebra Desalting Columns). CHOK1 and CHO745 cells were maintained in F-12 media supplemented with 10% fetal calf serum and 100× penicillin/streptomycin. On the day of the experiment, cells were washed once with PBS, detached using 0.2% EDTA, and resuspended in staining buffer containing PBS, 1% BSA, and 2 mM EDTA. Biotinylated CCL2 was added to cells at a final concentration of 50 nM in the presence or absence of $R17^{GAG1}$ or $R17^{GAG2}$, incubated for 1 hr on ice, washed three times, and detected with streptavidin PE (Life Technologies) using a FACSCalibur (BD Biosciences).

SPR Binding Analysis

SPR was used to directly measure the affinity and kinetics of chemokine binding by R17 and its variants, and is described in Lubman et al. (2014). In brief, R17 was immobilized to on a CM5 chip (GE Healthcare) using standard amine coupling chemistry (BIAcore Amine coupling kit) to a level of 200–500 response units for kinetic binding analysis using a BIAcore T-100 biosensor (GE Healthcare). A control flow cell was prepared by coupling a non-chemokine binding protein R7 or neutravidin to the chip at similar level.

Recombinant Chemokines

Mutagenesis of mouse CCL2 residues Leu46 to Arg and Lys47 to Asn was performed using a Multi-Site Quick Change Mutagenesis Kit (Agilent Technologies) on the background of the wild-type mouse CCL2 and verified by DNA sequencing. Murine CCL2, $CCL2^{L46R}$, $CCL2^{K47N}$, and $CCL2^{L46R\ K47N}$ were expressed in *E. coli*, refolded from inclusion bodies, and purified as previously described (Nelson et al., 2014).

SUPPLEMENTAL INFORMATION

Supplemental Information includes two figures and can be found with this article online at http://dx.doi.org/10.1016/j.str.2015.10.018.

AUTHOR CONTRIBUTIONS

O.L. and D.H.F. conceived the study and designed experiments, performed experiments and analysis, and wrote and edited the manuscript.

ACKNOWLEDGMENTS

The authors would like to thank J. Nix at ALS beamline 4.2.2 (Lawrence Berkeley Laboratories) for help with X-ray data collection, and the APS CCP4 School for help with iodide anomalous signal calculation and data collection at macromolecular crystallography beamline 23ID-D. We thank Chris Nelson for discussions and careful reading of the manuscript. This work was supported by the Washington University/Pfizer Biomedical Agreement, the Center for Women's Infectious Disease Research (cWIDR), and NIAID grants R01 AI019687 and U54 AI057160.

Received: May 13, 2015
Revised: October 16, 2015
Accepted: October 20, 2015
Published: December 3, 2015

REFERENCES

Adams, P.D., Afonine, P.V., Bunkoczi, G., Chen, V.B., Echols, N., Headd, J.J., Hung, L.W., Jain, S., Kapral, G.J., Grosse Kunstleve, R.W., et al. (2011). The Phenix software for automated determination of macromolecular structures. Methods *55*, 94–106.

Alcami, A. (2003). Viral mimicry of cytokines, chemokines and their receptors. Nat. Rev. Immunol. *3*, 36–50.

Alcami, A., and Lira, S.A. (2010). Modulation of chemokine activity by viruses. Curr. Opin. Immunol. *22*, 482–487.

Alexander, J.M., Nelson, C.A., van Berkel, V., Lau, E.K., Studts, J.M., Brett, T.J., Speck, S.H., Handel, T.M., Virgin, H.W., and Fremont, D.H. (2002). Structural basis of chemokine sequestration by a herpesvirus decoy receptor. Cell *111*, 343–356.

Alexander-Brett, J.M., and Fremont, D.H. (2007). Dual GPCR and GAG mimicry by the M3 chemokine decoy receptor. J. Exp. Med. *204*, 3157–3172.

Allen, S.J., Crown, S.E., and Handel, T.M. (2007). Chemokine: receptor structure, interactions, and antagonism. Annu. Rev. Immunol. *25*, 787–820.

Burg, J.S., Ingram, J.R., Venkatakrishnan, A.J., Jude, K.M., Dukkipati, A., Feinberg, E.N., Angelini, A., Waghray, D., Dror, R.O., Ploegh, H.L., et al. (2015). Structural biology. Structural basis for chemokine recognition and activation of a viral G protein-coupled receptor. Science *347*, 1113–1117.

Chang, V.T., Crispin, M., Aricescu, A.R., Harvey, D.J., Nettleship, J.E., Fennelly, J.A., Yu, C., Boles, K.S., Evans, E.J., Stuart, D.I., et al. (2007). Glycoprotein structural genomics: solving the glycosylation problem. Structure *15*, 267–273.

Cianci, M., Helliwell, J.R., and Suzuki, A. (2008). The interdependence of wavelength, redundancy and dose in sulfur SAD experiments. Acta Crystallogr. D Biol. Crystallogr. *64*, 1196–1209.

Clambey, E.T., Virgin, H.W., 4th, and Speck, S.H. (2000). Disruption of the murine gammaherpesvirus 68 M1 open reading frame leads to enhanced reactivation from latency. J. Virol. *74*, 1973–1984.

Clark-Lewis, I., Kim, K.S., Rajarathnam, K., Gong, J.H., Dewald, B., Moser, B., Baggiolini, M., and Sykes, B.D. (1995). Structure-activity relationships of chemokines. J. Leukoc. Biol. *57*, 703–711.

Cowtan, K. (2010). Recent developments in classical density modification. Acta Crystallogr. D Biol. Crystallogr. *66*, 470–478.

Czaplewski, L.G., McKeating, J., Craven, C.J., Higgins, L.D., Appay, V., Brown, A., Dudgeon, T., Howard, L.A., Meyers, T., Owen, J., et al. (1999). Identification of amino acid residues critical for aggregation of human CC chemokines macrophage inflammatory protein (MIP)-1alpha, MIP-1beta, and RANTES. Characterization of active disaggregated chemokine variants. J. Biol. Chem. *274*, 16077–16084.

Deruaz, M., Frauenschuh, A., Alessandri, A.L., Dias, J.M., Coelho, F.M., Russo, R.C., Ferreira, B.R., Graham, G.J., Shaw, J.P., Wells, T.N., et al. (2008). Ticks produce highly selective chemokine binding proteins with antiinflammatory activity. J. Exp. Med. *205*, 2019–2031.

Dias, J.M., Losberger, C., Deruaz, M., Power, C.A., Proudfoot, A.E., and Shaw, J.P. (2009). Structural basis of chemokine sequestration by a tick chemokine binding protein: the crystal structure of the complex between Evasin-1 and CCL3. PLoS One *4*, e8514.

Dodson, E.J., Winn, M., and Ralph, A. (1997). Collaborative Computational Project, number 4: providing programs for protein crystallography. Methods Enzymol. *277*, 620–633.

Elbein, A.D., Kerbacher, J.K., Schwartz, C.J., and Sprague, E.A. (1991). Kifunensine inhibits glycoprotein processing and the function of the modified LDL receptor in endothelial cells. Arch. Biochem. Biophys. *288*, 177–184.

Emsley, P., and Cowtan, K. (2004). Coot: model-building tools for molecular graphics. Acta Crystallogr. D Biol. Crystallogr. *60*, 2126–2132.

Epperson, M.L., Lee, C.A., and Fremont, D.H. (2012). Subversion of cytokine networks by virally encoded decoy receptors. Immunol. Rev. *250*, 199–215.

Esche, C., Stellato, C., and Beck, L.A. (2005). Chemokines: key players in innate and adaptive immunity. J. Invest. Dermatol. *125*, 615–628.

Evans, A.G., Moorman, N.J., Willer, D.O., and Speck, S.H. (2006). The M4 gene of gammaHV68 encodes a secreted glycoprotein and is required for the efficient establishment of splenic latency. Virology *344*, 520–531.

Fernandez, E.J., and Lolis, E. (2002). Structure, function, and inhibition of chemokines. Annu. Rev. Pharmacol. Toxicol. *42*, 469–499.

Frauenschuh, A., Power, C.A., Deruaz, M., Ferreira, B.R., Silva, J.S., Teixeira, M.M., Dias, J.M., Martin, T., Wells, T.N., and Proudfoot, A.E. (2007). Molecular cloning and characterization of a highly selective chemokine-binding protein from the tick Rhipicephalus sanguineus. J. Biol. Chem. *282*, 27250–27258.

Gerard, C., and Rollins, B.J. (2001). Chemokines and disease. Nat. Immunol. *2*, 108–115.

Graham, K.A., Lalani, A.S., Macen, J.L., Ness, T.L., Barry, M., Liu, L.Y., Lucas, A., Clark-Lewis, I., Moyer, R.W., and McFadden, G. (1997). The T1/35kDa

family of poxvirus-secreted proteins bind chemokines and modulate leukocyte influx into virus-infected tissues. Virology *229*, 12–24.

Handel, T.M., and Lau, E.K. (2004). Chemokine structure and receptor interactions. Ernst Schering Res. Found. Workshop *45*, 101–124.

Handel, T.M., Johnson, Z., Crown, S.E., Lau, E.K., and Proudfoot, A.E. (2005). Regulation of protein function by glycosaminoglycans—as exemplified by chemokines. Annu. Rev. Biochem. *74*, 385–410.

Heidarieh, H., Hernaez, B., and Alcami, A. (2015). Immune modulation by virus-encoded secreted chemokine binding proteins. Virus Res. *209*, 65–75.

Holm, L., and Sander, C. (1995). Dali: a network tool for protein structure comparison. Trends Biochem. Sci. *20*, 478–480.

Kim, S., Jao, S., Laurence, J.S., and LiWang, P.J. (2001). Structural comparison of monomeric variants of the chemokine MIP-1beta having differing ability to bind the receptor CCR5. Biochemistry *40*, 10782–10791.

Koopmann, W., Ediriwickrema, C., and Krangel, M.S. (1999). Structure and function of the glycosaminoglycan binding site of chemokine macrophage-inflammatory protein-1 beta. J. Immunol. *163*, 2120–2127.

Krmpotic, A., Hasan, M., Loewendorf, A., Saulig, T., Halenius, A., Lenac, T., Polic, B., Bubic, I., Kriegeskorte, A., Pernjak-Pugel, E., et al. (2005). NK cell activation through the NKG2D ligand MULT-1 is selectively prevented by the glycoprotein encoded by mouse cytomegalovirus gene m145. J. Exp. Med. *201*, 211–220.

Kufareva, I., Salanga, C.L., and Handel, T.M. (2015). Chemokine and chemokine receptor structure and interactions: implications for therapeutic strategies. Immunol. Cell Biol. *93*, 372–383.

Laurence, J.S., Blanpain, C., Burgner, J.W., Parmentier, M., and LiWang, P.J. (2000). CC chemokine MIP-1 beta can function as a monomer and depends on Phe13 for receptor binding. Biochemistry *39*, 3401–3409.

Lawrence, M.C., and Colman, P.M. (1993). Shape complementarity at protein/protein interfaces. J. Mol. Biol. *234*, 946–950.

Lee, H.R., Amatya, R., and Jung, J.U. (2015). Multi-step regulation of innate immune signaling by Kaposi's sarcoma-associated herpesvirus. Virus Res. *209*, 39–44.

Lodoen, M.B., Abenes, G., Umamoto, S., Houchins, J.P., Liu, F., and Lanier, L.L. (2004). The cytomegalovirus m155 gene product subverts natural killer cell antiviral protection by disruption of H60-NKG2D interactions. J. Exp. Med. *200*, 1075–1081.

Loh, J., Zhao, G., Nelson, C.A., Coder, P., Droit, L., Handley, S.A., Johnson, L.S., Vachharajani, P., Guzman, H., Tesh, R.B., et al. (2011). Identification and sequencing of a novel rodent gammaherpesvirus that establishes acute and latent infection in laboratory mice. J. Virol. *85*, 2642–2656.

Lubman, O.Y., and Waksman, G. (2002). Dissection of the energetic coupling across the Src SH2 domain-tyrosyl phosphopeptide interface. J. Mol. Biol. *316*, 291–304.

Lubman, O.Y., Cella, M., Wang, X., Monte, K., Lenschow, D.J., Huang, Y.H., and Fremont, D.H. (2014). Rodent herpesvirus Peru encodes a secreted chemokine decoy receptor. J. Virol. *88*, 538–546.

Luster, A.D. (1998). Chemokines—chemotactic cytokines that mediate inflammation. N. Engl. J. Med. *338*, 436–445.

Minor, W., Cymborowski, M., Otwinowski, Z., and Chruszcz, M. (2006). HKL-3000: the integration of data reduction and structure solution–from diffraction images to an initial model in minutes. Acta Crystallogr. D Biol. Crystallogr. *62*, 859–866.

Molina, H., Holers, V.M., Li, B., Fung, Y., Mariathasan, S., Goellner, J., Strauss-Schoenberger, J., Karr, R.W., and Chaplin, D.D. (1996). Markedly impaired humoral immune response in mice deficient in complement receptors 1 and 2. Proc. Natl. Acad. Sci. USA *93*, 3357–3361.

Murshudov, G.N., Vagin, A.A., and Dodson, E.J. (1997). Refinement of macromolecular structures by the maximum-likelihood method. Acta Crystallogr. D Biol. Crystallogr. *53*, 240–255.

Nelson, C.A., Lee, C.A., and Fremont, D.H. (2014). Oxidative refolding from inclusion bodies. Methods Mol. Biol. *1140*, 145–157.

Nemerow, G.R., Mold, C., Schwend, V.K., Tollefson, V., and Cooper, N.R. (1987). Identification of gp350 as the viral glycoprotein mediating attachment of Epstein-Barr virus (EBV) to the EBV/C3d receptor of B cells: sequence homology of gp350 and C3 complement fragment C3d. J. Virol. *61*, 1416–1420.

O'Flaherty, B.M., Soni, T., Wakeman, B.S., and Speck, S.H. (2014). The murine gammaherpesvirus immediate-early Rta synergizes with IRF4, targeting expression of the viral M1 superantigen to plasma cells. PLoS Pathog. *10*, e1004302.

Patel, A.H., Gaffney, D.F., Subak-Sharpe, J.H., and Stow, N.D. (1990). DNA sequence of the gene encoding a major secreted protein of vaccinia virus, strain Lister. J. Gen. Virol. *71*, 2013–2021.

Pease, J.E., Wang, J., Ponath, P.D., and Murphy, P.M. (1998). The N-terminal extracellular segments of the chemokine receptors CCR1 and CCR3 are determinants for MIP-1alpha and eotaxin binding, respectively, but a second domain is essential for efficient receptor activation. J. Biol. Chem. *273*, 19972–19976.

Proudfoot, A.E., Bonvin, P., and Power, C.A. (2015). Targeting chemokines: pathogens can, why can't we? Cytokine *74*, 259–267.

Qin, L., Kufareva, I., Holden, L.G., Wang, C., Zheng, Y., Zhao, C., Fenalti, G., Wu, H., Han, G.W., Cherezov, V., et al. (2015). Crystal structure of the chemokine receptor CXCR4 in complex with a viral chemokine. Science *347*, 1117–1122.

Schneider, T.R., and Sheldrick, G.M. (2002). Substructure solution with SHELXD. Acta Crystallogr. D Biol. Crystallogr. *58*, 1772–1779.

Sheldrick, G.M. (2008). A short history of SHELX. Acta Crystallogr. A *64*, 112–122.

Smith, C.A., Smith, T.D., Smolak, P.J., Friend, D., Hagen, H., Gerhart, M., Park, L., Pickup, D.J., Torrance, D., Mohler, K., et al. (1997). Poxvirus genomes encode a secreted, soluble protein that preferentially inhibits beta chemokine activity yet lacks sequence homology to known chemokine receptors. Virology *236*, 316–327.

Smith, P., Fallon, R.E., Mangan, N.E., Walsh, C.M., Saraiva, M., Sayers, J.R., McKenzie, A.N., Alcami, A., and Fallon, P.G. (2005). *Schistosoma mansoni* secretes a chemokine binding protein with antiinflammatory activity. J. Exp. Med. *202*, 1319–1325.

Stevenson, P.G., and Efstathiou, S. (2005). Immune mechanisms in murine gammaherpesvirus-68 infection. Viral Immunol. *18*, 445–456.

Szakonyi, G., Klein, M.G., Hannan, J.P., Young, K.A., Ma, R.Z., Asokan, R., Holers, V.M., and Chen, X.S. (2006). Structure of the Epstein-Barr virus major envelope glycoprotein. Nat. Struct. Mol. Biol. *13*, 996–1001.

Teng, M.S., Shadbolt, P., Fraser, A.G., Jansen, G., and McCafferty, J. (2008). Control of feeding behavior in *C. elegans* by human G protein-coupled receptors permits screening for agonist-expressing bacteria. Proc. Natl. Acad. Sci. USA *105*, 14826–14831.

van Berkel, V., Barrett, J., Tiffany, H.L., Fremont, D.H., Murphy, P.M., McFadden, G., Speck, S.H., and Virgin, H.I. (2000). Identification of a gammaherpesvirus selective chemokine binding protein that inhibits chemokine action. J. Virol. *74*, 6741–6747.

Wang, D., Bresnahan, W., and Shenk, T. (2004). Human cytomegalovirus encodes a highly specific RANTES decoy receptor. Proc. Natl. Acad. Sci. USA *101*, 16642–16647.

Wang, R., Natarajan, K., Revilleza, M.J., Boyd, L.F., Zhi, L., Zhao, H., Robinson, H., and Margulies, D.H. (2012). Structural basis of mouse cytomegalovirus m152/gp40 interaction with RAE1gamma reveals a paradigm for MHC/MHC interaction in immune evasion. Proc. Natl. Acad. Sci. USA *109*, E3578–E3587.

Wu, X., Jiang, N., Fang, Y.F., Xu, C., Mao, D., Singh, J., Fu, Y.X., and Molina, H. (2000). Impaired affinity maturation in Cr2-/- mice is rescued by adjuvants without improvement in germinal center development. J. Immunol. *165*, 3119–3127.

Yogavel, M., Gill, J., Mishra, P.C., and Sharma, A. (2007). SAD phasing of a structure based on cocrystallized iodides using an in-house Cu Kalpha X-ray

source: effects of data redundancy and completeness on structure solution. Acta Crystallogr. D Biol. Crystallogr. *63*, 931–934.

Yogavel, M., Gill, J., and Sharma, A. (2009). Iodide-SAD, SIR and SIRAS phasing for structure solution of a nucleosome assembly protein. Acta Crystallogr. D Biol. Crystallogr. *65*, 618–622.

Zhang, L., Derider, M., McCornack, M.A., Jao, S.C., Isern, N., Ness, T., Moyer, R., and LiWang, P.J. (2006). Solution structure of the complex between poxvirus-encoded CC chemokine inhibitor vCCI and human MIP-1beta. Proc. Natl. Acad. Sci. USA *103*, 13985–13990.

Zhi, L., Mans, J., Paskow, M.J., Brown, P.H., Schuck, P., Jonjic, S., Natarajan, K., and Margulies, D.H. (2010). Direct interaction of the mouse cytomegalovirus m152/gp40 immunoevasin with RAE-1 isoforms. Biochemistry *49*, 2443–2453.